

Study of Fracture Permeability Using Lattice Gas Automata

R. GUTFRAIN^{*} and A. HANSEN^{**}

Groupe Matière Condensée et Matériaux, URA CNRS 804, Université de Rennes 1, Bât. 11B, Campus de Beaulieu, F-35042 Rennes Cedex, France

(Received: 11 January 1994; in final form: 20 June 1994)

Abstract. We study the problem of flow permeability of fracture joints using Lattice-Gas Automata simulations. We model the fracture as a rough channel bounded by a self-affine surface. Changing the surface roughness exponent, rough walls having different microstructures are obtained. Different relative roughnesses – defined as the height of the largest surface asperity divided by the mean aperture – are obtained ‘pulling apart’ the two surfaces that constitute the rough walls of the channel. We calculate the macroscopic variables volume flow rate and pressure difference using microscopic balances. In the low Reynolds number regime the pressure difference and the flow rate are linearly related (the behavior is described by Darcy’s law). In this regime, we study the effect of geometry on the permeability. We have found that permeability is independent of the surface roughness exponent H and it is fully determined in terms of the relative roughness and mean aperture of the fracture joint. For larger Reynolds numbers a transition to a regime in which pressure difference and flow rate are not longer linearly related is observed. This transition is observed in a domain of Reynolds numbers for which the behavior in a smooth channel remains linear. We discuss this transition.

Key words: Permeability, self-affine, fractures, lattice-gas.

1. Introduction

Many of the surfaces one usually finds in nature are highly fractured on all scales, ranging from microcracks to large scale joints and faults. Over the past few years considerably progress has been achieved in the characterization of fracture surface morphology, in which scale invariance, in the form of *self affinity*, was found in widely different materials ranging from crystalline materials on the nanometer scale to natural fault and rock surfaces up to and beyond the meter scale [1–15] – for recent reviews, see Reference [16]. Surface geometry controls the fracture permeability since the fracture aperture is related to the roughness of the two surfaces in contact. The problem of flow permeability through fractured joints is of primary importance in fields such as petroleum engineering, geology and hydrology.

In this paper we model the fracture as a rough channel bounded by self-affine surfaces [17] and we use the Lattice-Gas Automaton (LGA) for hydrodynamics

^{*} Present Address: Department of Civil Engineering and Applied Mechanics, McGill University, H3A 2K6 Montreal, Canada.

^{**} Also at Institutt for fysikk, NTH, N-7034 Trondheim, Norway.

developed by Frisch, Hasslacher and Pomeau (FHP) [18] to study flow permeability. This model has already been successfully applied to study several problems, including flow in porous media [19], osmotic flow across semipermeable porous membranes [20], models with surface tension for simulations of immiscible two phase flows [21, 22] and boundary layer problems [23]. The model is particularly appropriate for studying hydrodynamics in environments with complex boundaries rendering boundary conditions very difficult to implement using other methods, such as finite difference schemes.

Flow through porous media or fractures is usually described using Darcy law

$$Q = \frac{KA \Delta P}{\rho \nu L}, \quad (1)$$

where Q is the volume flow rate, ΔP is the pressure difference between measuring points separated a distance L , ν is the kinematic viscosity of the liquid, ρ the fluid density, A is the flow cross section and K is the permeability which is a function of the pore geometry only. In several applications fluid flow through a single fracture is assumed analogous to laminar flow between two smooth plates,

$$Q = \frac{\delta^3 \Delta P}{12\rho\nu L}, \quad (2)$$

where δ is the separation between the plates. In this case the permeability K is given by $\delta^2/12$. Theoretical approaches have usually focused on redefining the aperture term in the cubic law in order to account for the surface roughness and the tortuosity of the path, see e.g. references [24, 25].

Brown [26] studied the effect of roughness in the flow through fractured joints solving Reynolds equation (this equation is used to describe the flow between slightly nonparallel and nonplanar surfaces). For various surface roughnesses (in his language, ‘fractal dimensions’) Brown calculated the hydrodynamic conductance as a function of the root-mean square of the surface height. Roux *et al.* [27] recently suggested that the Hydraulic Conductance of a fractured joint has to scale as l^{3H} , where l is the displacement of the fracture parallel to the mean fracture plane and H is its roughness or Hurst exponent. This approach supposes that the ‘cubic law’ remains valid despite the self-affine surface roughness and this is used to estimate the mean separation between the two surfaces in terms of the horizontal displacement l . However, once one knows the mean separation, an additional factor accounting for the roughness has to be introduced in order to estimate the flow permeability: it is not enough to know the roughness exponent H only. Here we study these geometry effects on the permeability.

The paper is organized as follows: In Section 2 we introduce the LGA model for hydrodynamics and in Section 3 we present the simulations we have done in order to test the algorithm. In Section 4 we briefly discuss about the features of self-affine sets, we present the numerical results concerning the permeability of

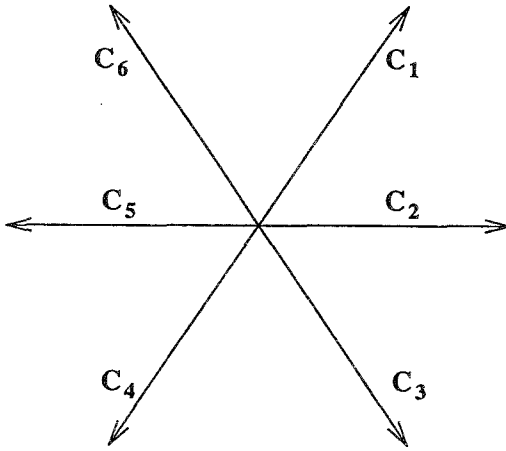


Fig. 1. The particle velocities c_i are numbered from 1 to 6 and all have module 1 (c_0 is a particle at rest).

fracture joints and we discuss about the appropriateness of LGA to treat this type of problems. In Section 5 we discuss the observed non-linear effects.

2. Lattice-Gas Automata

We now briefly summarize the main features of the lattice gas cellular automaton (LGA) model (for details see Reference [28]). The residing lattice is triangular which ensures the isotropy of the relevant fourth order tensor. The fluid is represented by a set of identical boolean particles with discrete velocities. The particles can have either a velocity of unit value along one of the six directions of the lattice or be at rest on a node of the lattice, see Figure 1. This multiply occupancy of a lattice node is subject to a constraint, the exclusion principle which states that at a given node no two particles can have the same velocity. Therefore a lattice node can be empty or occupied up to a maximum of seven particles. The time evolution of the system proceeds in two steps: propagation and collision. During the propagation step, each particle moves one lattice unit in a direction determined by its velocity or it stays at rest. In the collision step, particles undergo instantaneous collisions at the lattice nodes during which their velocities are modified according to the collision rules. These collisions obey conservation of mass and momentum. The model FHP I uses only six possible velocities and all their collision rules are given in Figure 2a. The model we use here is FHP II which also includes rest and moving-particle collisions, see Figure 2b. When more than 3 particles coexist on the same lattice node no collision occurs.

The state of the lattice gas is fully determined by the specification for each site r_j of seven boolean variables $n_i(r_j)$ ($i = 0, 1, \dots, 6$). $n_i(r_j)$ is equal to 0 or 1 depending on the presence ($n_i = 1$) or absence ($n_i = 0$) at the site r_j of a particle

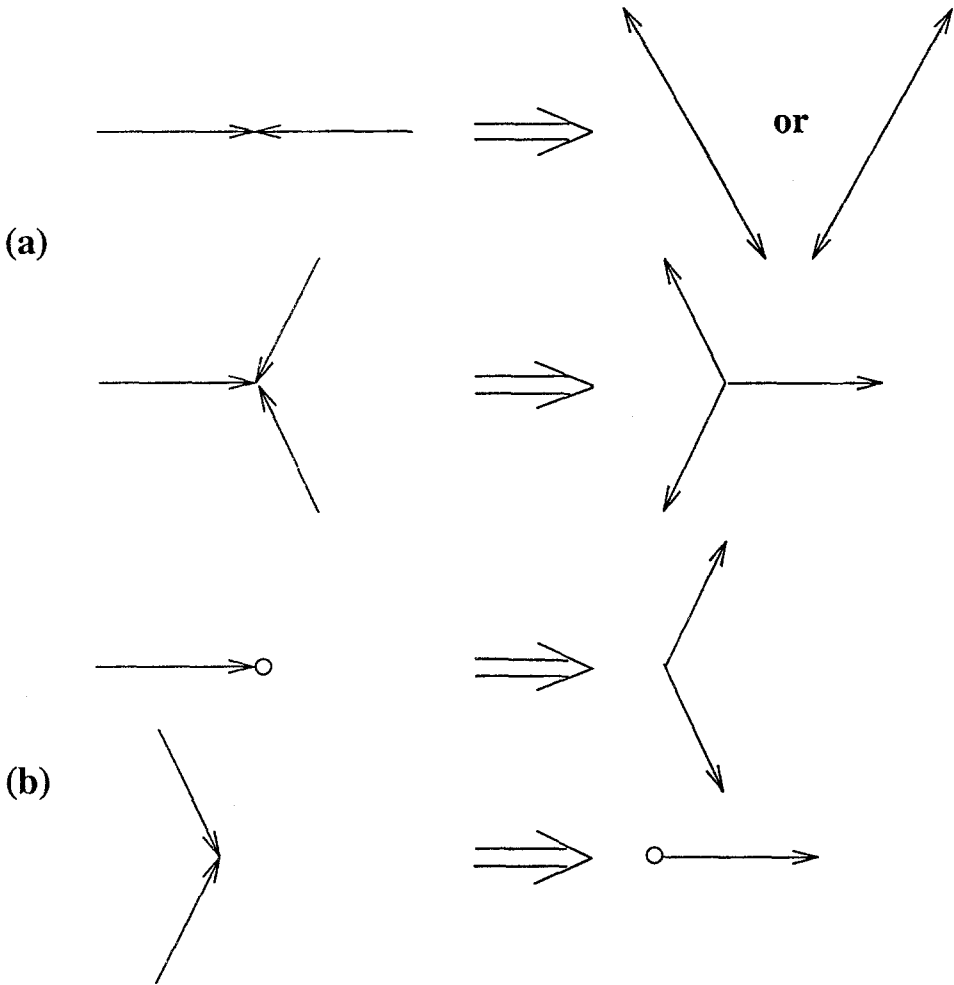


Fig. 2. (a) All allowed binary and triple collisions in the FHP I model. (b) Additional collisions including rest particles (FHP II model). All these collisions conserve both momentum and particle number.

with its velocity oriented along direction i ($i = 0$ corresponds to a particle at rest). In terms of their ensemble average, $N_i = \langle n_i \rangle$, one defines macroscopic quantities such as the average mass and momentum density per site ρ and $\rho \mathbf{u}$ [28],

$$\rho = \sum_i N_i \tag{3a}$$

and

$$\rho \mathbf{u} = \sum_i N_i \mathbf{c}_i, \tag{3b}$$

respectively. Here \mathbf{c}_i where $i = 1, \dots, 6$ are the velocity vectors defined in Figure 1, and $\mathbf{c}_0 = \mathbf{0}$.

It can be shown that for small velocities \mathbf{u} the system obeys the Navier–Stokes equation with a correction term [28]:

$$\frac{\partial \mathbf{u}}{\partial t} + g(\rho)(\mathbf{u} \cdot \nabla)\mathbf{u} = -\nabla P + \nu \nabla^2 \mathbf{u}, \quad (4)$$

where $g(\rho)$ is the mentioned correction term. For the FHP II model $g(\rho)$ is given by [29]

$$g(\rho) = \frac{7}{12} \frac{(2\rho - 7)}{(\rho - 7)}. \quad (5)$$

The term $g(\rho)$ restricts the use of lattice-gas models to incompressible flows. In this case, ρ is constant and then $g(\rho)$ is also a constant that can be absorbed in a rescaled velocity. This model leads to the following expression for the kinematic viscosity of the gas [29],

$$\nu = \frac{1}{28d(1-d)^3(1-4d/7)} - \frac{1}{8}. \quad (6)$$

Note that ν is defined as a ‘kinematic viscosity’ relative to the density ρ which is a density per site. We shall use this expression to test the numerical algorithm.

3. Numerical Verification of the Algorithm

The most common method for programming lattice-gas automata is through look-up tables. A detailed description of how to program LGA using this method can be found in Reference [30]. In order to use this algorithm the state of each lattice site is put in one computer word. For the FHP II model this can be done using words of 8 bits. For instance, the configuration of a site having particles with velocity \mathbf{c}_0 (a particle at rest), \mathbf{c}_2 and \mathbf{c}_4 is stored in the computer as $2^0 + 2^2 + 2^4$. The eighth bit can be used to indicate whether or not the lattice site is a boundary site.

In order to test the algorithm we simulate the flow through a two-dimensional channel. The channel is a rectangle with one of its sides parallel to the flow direction. The equilateral triangles of the lattice have one of its sides parallel to the flow direction. The side of the elementary triangles is taken as the lattice constant of the lattice. Initially, particles are distributed on the lattice with the same probability of being at rest or of having a unit value velocity in one of the six lattice directions. At both ends of the channel periodic boundary conditions are imposed, particles leaving the channel at the right end are reinserted at the left one in order to maintain the number of particles constant. In order to implement no-slip boundary conditions, particles incoming to the boundary simple bounce-back into the direction from which they came (Figure 3). This rule ensures that,

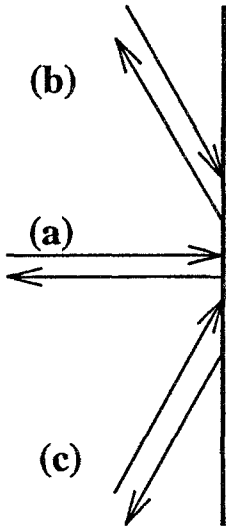


Fig. 3. Particle reflection upon collision with a frictional wall. These rules ensure a vanishing velocity in both the normal and parallel direction to the wall.

on the average, there is no local relative velocity of the fluid with respect to the solid walls. This constraint creates a viscous dissipation which is compensated in our simulations by a 'gravitational force' [31] applied to the particles in the longitudinal direction (a constant mean velocity is thus maintained). This force is created by the forcing rules described in Figure 4. Note that all these rules ensure the application of a positive momentum only in the x -direction. Depending on the value of a parameter g ($0 < g < 1$) a given fraction of lattice sites are randomly chosen at each iteration and whenever is possible the forcing rules of Figure 4 are applied.

The applied force is estimated through equating momentum input and output in the system. Two methods are used for this: (a) We count the number of molecules of each velocity direction that are turned around at each iteration. When rule (a) – defined in Figure 4 – is applied the momentum gain in the x -direction is $2c_2$. When rules (b) or (c) are applied, the momentum gain is $2c_1 \cos(\pi/3) = c_1$ and $2c_3 \cos(\pi/3) = c_3$, respectively. The average moment gain per unit time (per iteration) is the applied force. (b) At steady state the applied force is equal to the frictional losses due to collisions with the wall (all the other collisions keep the momentum unchanged). Referring to Figure 3, in case (a) the momentum lost in the x -direction by the particle that collides with the surface is $2c_2$, whereas in (b) and (c), it is $2c_3 \cos(\pi/3) = c_3$ and $2c_1 \cos(\pi/3) = c_1$, respectively.

We first run a simulation with a fluid of density $\rho = 1$ in a channel of 600 lattice units length. The channel width is constituted by 100 elementary triangles which represents an effective cross section of $100\sqrt{3}/2$ lattice units. After 10000 steps the system reaches steady state. The velocity was then averaged over an additional

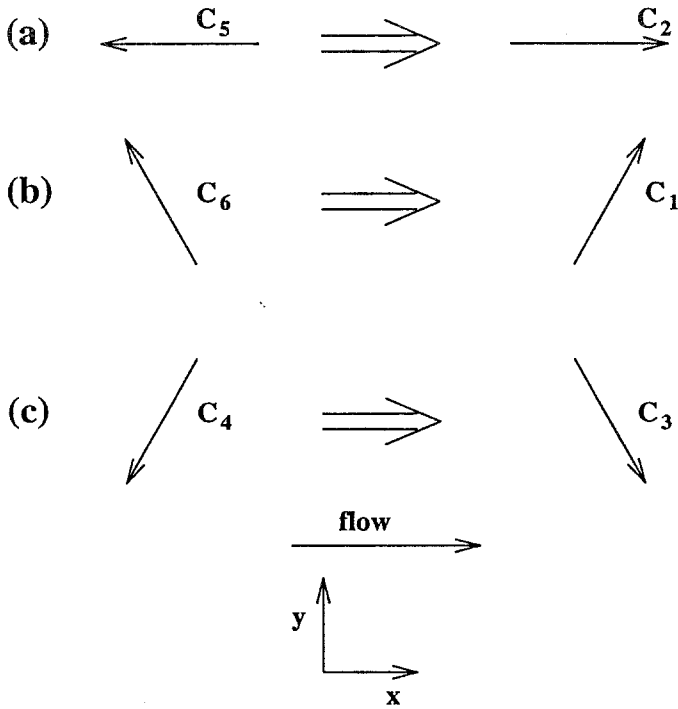


Fig. 4. The three microscopic forcing rules are shown as cases (a), (b) and (c). Each application of one of these rules adds momentum in the positive x -direction. In either case the momentum in the y -direction remains unchanged.

10000 steps and spatial averages were taken over boxes of 10×10 lattice units. Figure 5 shows the resulting velocity profile. One can see that the profile fits well the expected parabolic profile of a Poiseuille flow.

One can compare the viscosity obtained from the velocity profile of Figure 5 with that obtained from the Boltzmann approximation, Equation (6). In the present geometry the solution of the Navier–Stokes is given by Equation (2). ΔP is obtained from the simulations as the force, calculated using the rules described above, divided by the channel width. Figure 6 is obtained running simulations in a range of Reynolds number from 10 to 100, and from the slope we find $\nu = 0.30$. The value obtained substituting $d = 1/7$ in Equation (6) is $\nu = 0.31$, which is in good agreement with the value obtained from the simulations.

4. Permeability of Self-Affine Fractures

4.1. PROPERTIES OF SELF-AFFINE SURFACES

A set is self-affine if it is invariant under the affinity transformation [17]

$$x_i \rightarrow \lambda_i x_i. \tag{7}$$

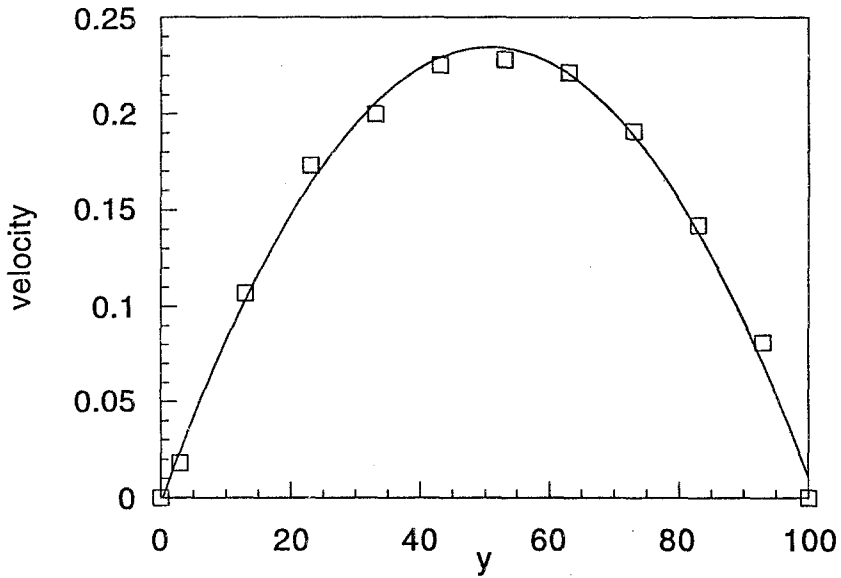


Fig. 5. Velocity profile after 20000 iteration steps. The squares represent averages over 10×10 boxes and 10000 iterations. The solid line is the best parabolic fit.

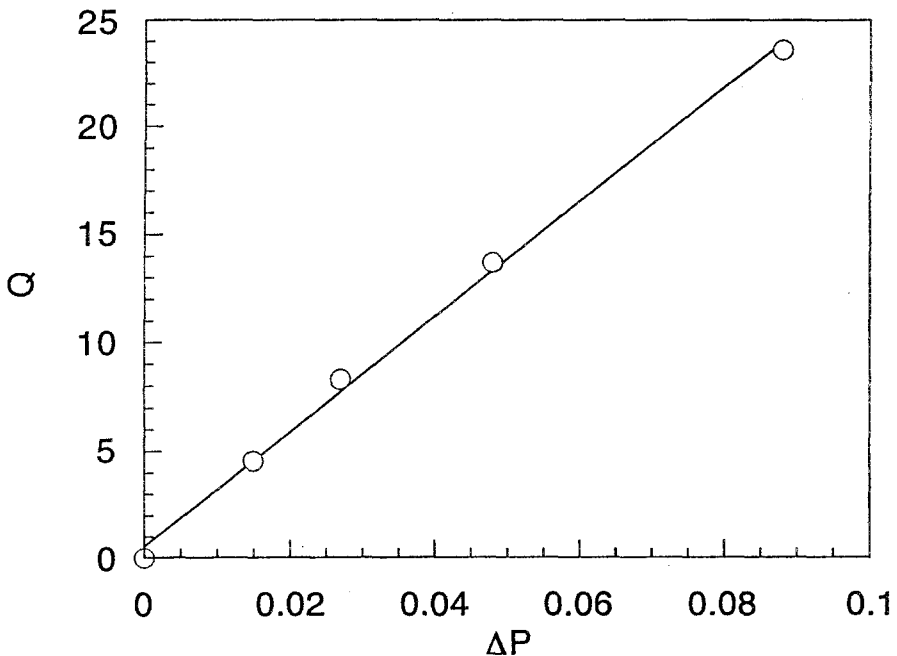


Fig. 6. Flow rate Q vs. pressure drop ΔP for a two-dimensional channel of 600 lattice units long. The range of flow-rates studied corresponds to a range of Reynolds numbers varying between 10 to 100. From the slope and Equation (2) one finds $\nu = 0.30$ in good agreement with the value $\nu = 0.31$ obtained from Equation (6).

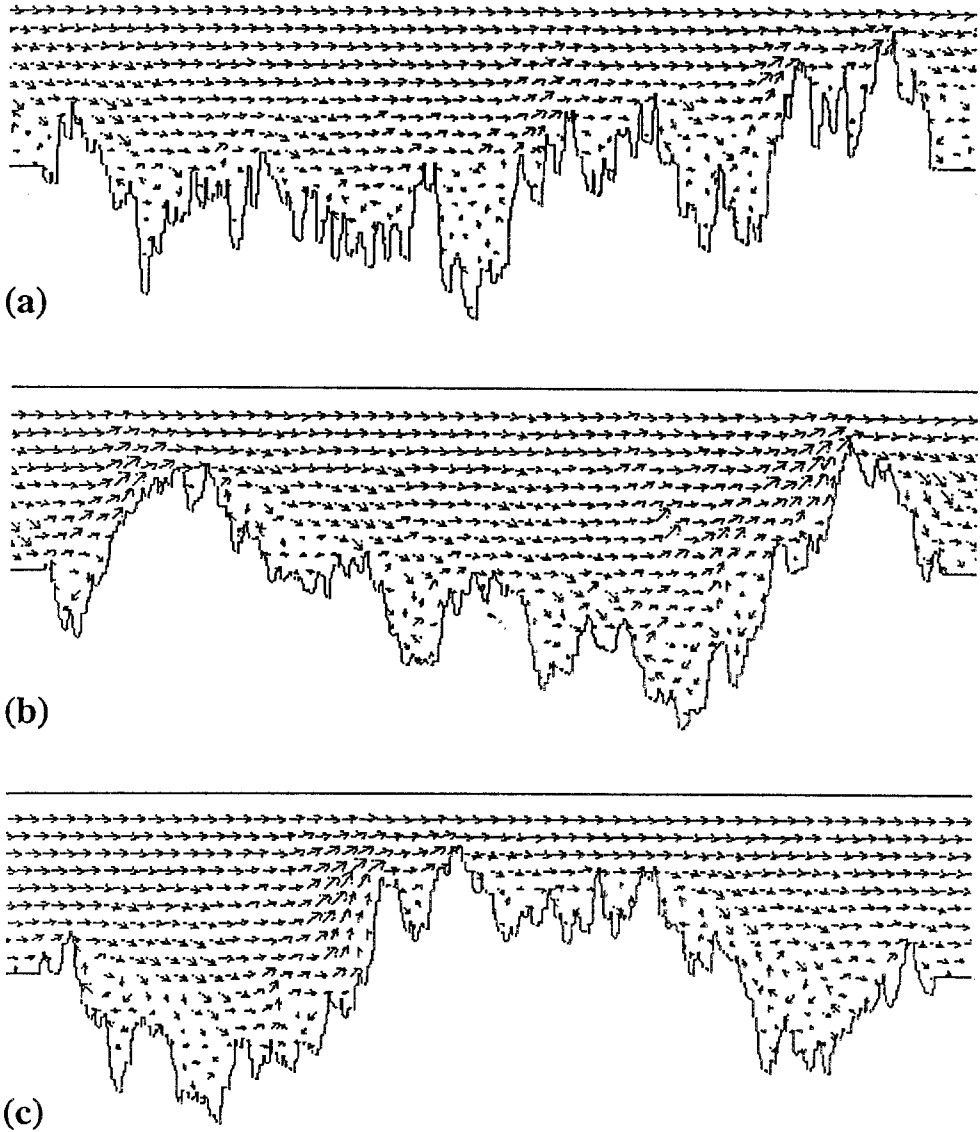


Fig. 7. The flow field in channels with rough boundaries. The roughness exponent is (a) $H = 0.3$, (b) $H = 0.5$ and (c) $H = 0.7$. The average aperture is $\delta_{av} = 240$ lattice units and the maximum height of the rough surface $y_{max} = 90$ lattice units. The upper boundary is a plane of symmetry. The flow lines are marked as arrows, whose lengths mark their strength on a logarithmic scale – see footnote in Section 4.2.

Group properties imply that all λ_i are homogeneous functions of one of the λ_i , e.g. $\lambda_i \sim \lambda_1^{h_i}$. In the case of the two-dimensional profiles used in this work (see Figure 7), this implies that

$$\lambda_2 \sim \lambda_1^{h_2}. \quad (8)$$

This is usually expressed in terms of the average width of the profile w (direction 2) and the profile length L (direction 1):

$$w \sim L^H, \quad (9)$$

where H is known as the Hurst or roughness exponent.

The algorithm used to generate these surfaces was proposed by Voss [32]. The algorithm uses an independent Gaussian variable ξ with zero mean and unit variance to determine the altitude of the points. For the one-dimensional profiles we use in this work, the algorithm can be summarized as follows: In the first generation the altitude of the central point ($x = 1/2$) is determined by generating one value for the Gaussian variable ξ . In the next generation the elevation for $x = 1/4$ is determined interpolating the elevation of $x = 0$ and $x = 1/2$; and the elevation of $x = 3/4$ interpolating the elevation for $x = 1/2$ and $x = 1$. Then one adds to these altitudes the value of the random variable $\xi_{n=1}$ which has now the variance

$$\langle \xi_n^2 \rangle = \frac{1}{r^{2nH}} \quad \text{with} \quad r = 1/\sqrt{2}.$$

In each generation, the algorithm doubles the number of positions at which the altitudes are specified, and reduces the distance between the points by a factor $1/\sqrt{2}$. The surfaces generated by this process are self affine on scales small compared to the linear size of the profile and they have a roughness exponent H . For details see Reference [17] or [32].

4.2. NUMERICAL ESTIMATION OF PERMEABILITY

In the simulations, the flow domain is a channel in which one of its sides is a rough self-affine surface and the other one is plane and parallel to the flow direction, as shown in Figure 7. The streamlines, which enables one to see the flow pattern near the wall are also shown.* We impose no-slip boundary conditions on the rough surface, and mirror-reflection type conditions on the smooth surface. Here, upon collision only one component of the particle momentum is changed, as this surface is a plane of symmetry on which $u_y = 0$ and $\partial u_x / \partial y = 0$.** This condition ensures maximum velocity on the x -direction and zero velocity on the y -direction. We also impose periodic boundary conditions in the flow direction.

* The strength of the flow field is shown on a logarithmic scale and is constructed as follows: The maximum length of an arrow is n lattice units and this corresponds to a velocity u that satisfies $u_{\max}/2 < u \leq u_{\max}$, $(n-1)$ lattice units corresponds to $u_{\max}/2^2 < u \leq u_{\max}/2$ and so on. This enables us to visualize the flow-field near the surface. In Figure 7 $n = 10$ lattice units.

** In this work we use mirror-reflection type boundary conditions, however, other boundary conditions, e.g. no slip can also be used. In both cases the distribution of widths in the fracture is self-affine. We are interested in the scaling properties of these surfaces and the presence of further symmetries, e.g. the symmetry plane, is irrelevant for this study.

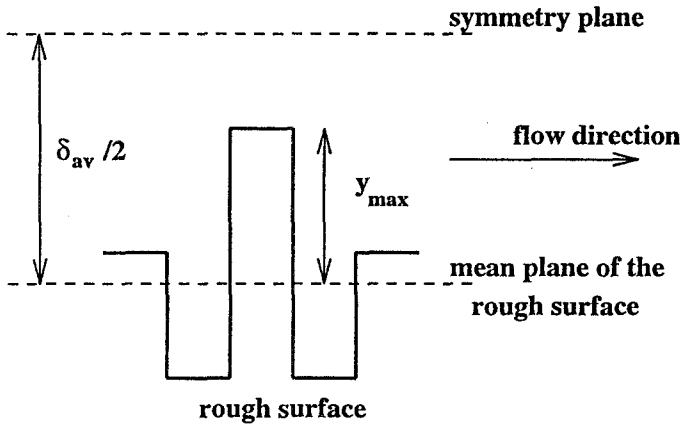


Fig. 8. Scheme of the rough channel. δ_{av} is the mean aperture of the fracture, namely twice the distance from the mean plane of the rough surface to the symmetry plane. y_{max} is the height of the largest surface peak.

We consider three values of the roughness exponent H : $H = 0.3$, $H = 0.5$ and $H = 0.7$, see Figure 7. For each H value we use two different surfaces. Besides the roughness exponent H , two other geometrical parameters are necessary to fully describe the system: the mean aperture δ_{av} and the height of the largest asperity of the rough surface y_{max} . The local aperture is twice the distance between the rough and the plane surface. The mean aperture δ_{av} is twice the distance between the smooth surface and the mean plane of the rough surface (see Figure 8).

In all the considered examples, $y_{max} \sim 90\sqrt{3}/2$ lattice units and δ_{av} varies from $\sim 200\sqrt{3}/2$ to $\sim 400\sqrt{3}/2$ lattice units. The three examples of Figure 7 have $\delta_{av} \sim 240$ lattice units. They have approximately the same mean aperture and relative roughness $y_{max}/(\delta_{av}/2)$. However, they have different microstructures, as lower roughness exponents lead to narrower pores. The linear size of the channels is 552 lattice units. This includes small smooth channels of 20 lattice units at each end (in the flow direction) of the channel. The fluid density per site $\rho = 1$, and its kinematic viscosity, calculated using Equation (6), is $\nu = 0.31$.

Tuning the parameter g (see Section 2) enables us to work at different flow rates. Between 20000 and 60000 iterations are required to stabilize the automata (depending on the value of δ_{av}). This time is of the order of δ_{av}^2/ν , the characteristic time for momentum diffusion. Each run takes between 20 to 40 minutes on a CRAY C98 depending on the system size and velocity.

From the simulations we get the flow rate Q and ΔP . The former is obtained averaging particle velocities over boxes of 10×10 lattice units and over 20000 iterations, and then calculating the flow rate across a channel section. ΔP is obtained as the force, calculated using the rules described in Section 3, divided by the channel width, the width being that of the smooth entrance and exit of the channel (see above). In each studied case, we first check that Q and ΔP

are linearly related. This is important as the roughness leads to a transition to a non-linear regime at much lower Reynolds numbers than in the case of smooth surfaces. In Figure 9 we show Q vs. ΔP for $H = 0.3$, $H = 0.5$ and $H = 0.7$. Two examples, corresponding to two relative roughness values for each H are presented. In Figure 9a $\delta_{av}/(2y_{max}) \sim 1.35$ and in Figure 9b $\delta_{av}/(2y_{max}) \sim 2.40$. For low Q values – i.e. low Reynolds numbers – Q and ΔP can be linearly fitted for all cases as it is shown in Figure 9. Notice that the slope is almost independent of the roughness exponent H . It has to be pointed out that the *origin* was included in all the fits and that the last point that already shows a large deviation from the linear fit was not included. These deviations from linearity are further discussed in Section 5.

From the slope at the origin we can then calculate the hydraulic diameter δ_H that satisfies

$$Q = \frac{\delta_H^3}{12\mu L} \Delta P. \quad (10)$$

Usually the mean aperture, δ_{av} , is used as an approximation for the hydraulic diameter, but predictions based on this approach are very far from experimental values, as well as from the simulation results we present here. This is shown in Figure 11, where $(\delta_H/\delta_{av})^3$ is plotted vs. $\delta_{av}/(2y_{max})$. Deviations from the simple Poiseuille flow based on the average aperture δ_{av} are accounted for using the geometrical parameter $\delta_{av}/(2y_{max})$. These deviations are fully determined by this parameter (and which are independent of the roughness exponent H) as can be seen in Figure 10 where the data for all the surfaces collapse on the same curve. Moreover, this curve can be well fitted as a power law of the form

$$(\delta_H/\delta_{av})^3 \sim 1 - \left(\frac{y_{max}}{\delta_{av}/2} \right)^\alpha, \quad (11)$$

with

$$\alpha \sim 0.35.$$

Note that Equation (11) satisfies the two asymptotic limits, for $y_{max}/(\delta_{av}/2) \rightarrow 0$ we find $(\delta_H/\delta_{av})^3 \sim 1$ and for $y_{max}/(\delta_{av}/2) \rightarrow 1$ we find $(\delta_H/\delta_{av})^3 \rightarrow 0$. One can see that once knowing the average aperture and the height of the largest asperity, the permeability is independent of the H value. This is because the largest asperities determine the flow pattern. One can easily see in Figure 7 that it is the largest pores which determine the effective cross section for the flow, and the smaller pores simply form recirculation or stagnation zones.

4.3. VALIDITY OF LGA FOR CHANNELS WITH ROUGH BOUNDARIES

As we have previously mentioned, we need to test the viability of LGA simulations to study problems of complex boundaries as the self-affine surfaces shown in Figure 7. One can expect here some of the same problems as observed in the study of

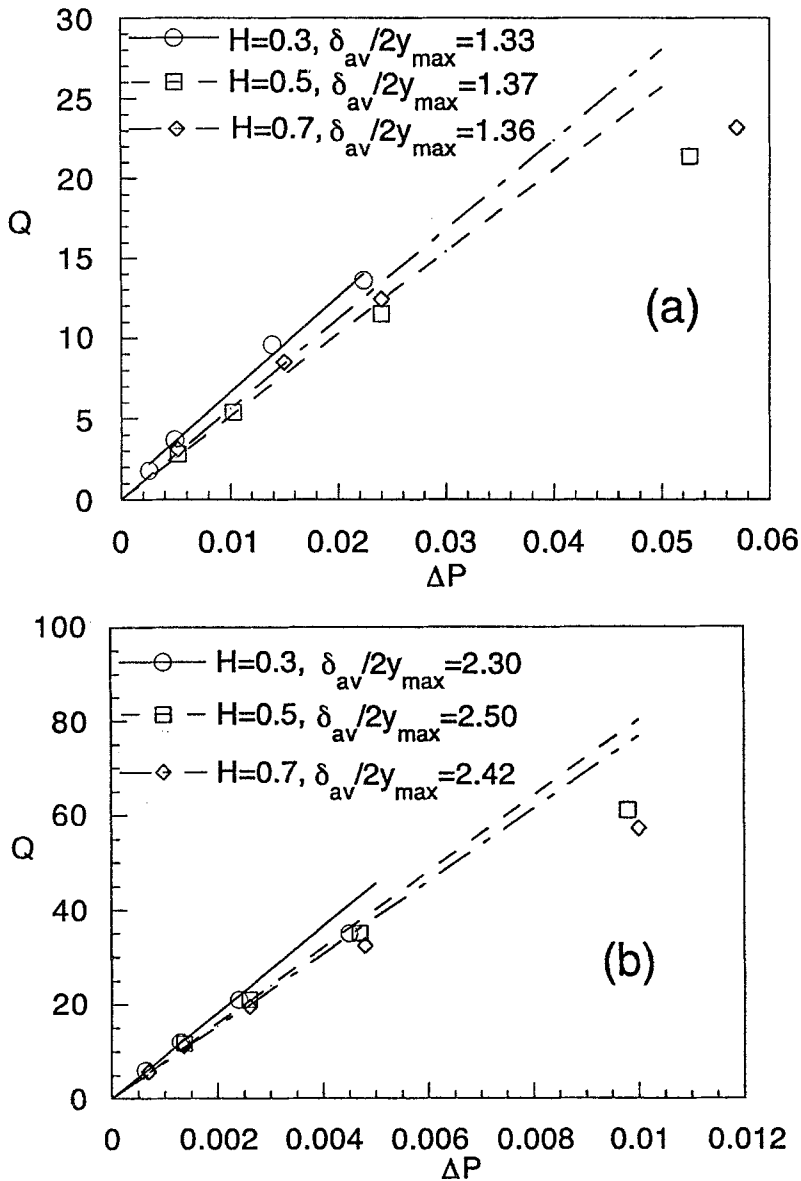


Fig. 9. ΔP vs. Q for rough channels of roughness exponent $H = 0.3$, $H = 0.5$ and $H = 0.7$, (a) the ratio $\delta_{av}/(2y_{max}) \sim 1.35$ and (b) $\delta_{av}/(2y_{max}) \sim 2.40$. For low Q values the data are linearly fitted. The origin is included in this fit. In both cases, (a) and (b), the last points deviate from the linear fit and are not included in it. Notice that the slope is almost independent of the roughness exponent H .

porous media using LGA simulations. Some authors have claimed that this technique is not appropriate when the mean free path of the cellular automata particles is of the order of magnitude of the pore size [19, 33]. In this case hydrodynamic

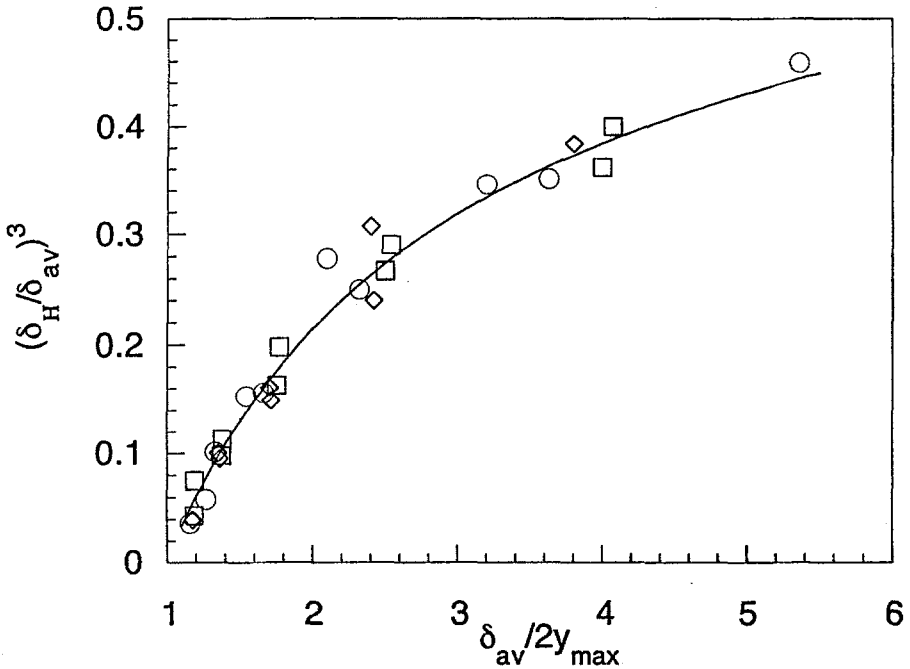


Fig. 10. $(\delta_H/\delta_{av})^3$ vs $\delta_{av}/(2y_{max})$. Circles are for the $H = 0.3$ surfaces, squares for $H = 0.5$ and diamonds for $H = 0.7$. The solid line is the best fit to the numerical results.

correlations cannot develop and the resulting flows will not be truly hydrodynamic. For a cellular-automaton fluid of $\rho = 1$ the mean free path has been estimated as $\lambda \sim 9$ lattice units. Thus, to have real hydrodynamic behavior, we expect the smallest pore size to be larger than 9 lattice units [34]. In the cases studied here, the rough surface is the boundary of the system and the small surface irregularities (or pores) have a negligible effect on the hydrodynamics. This is because the momentum losses are principally due to collisions with the singular points of the surface that are accessible through the largest pores.

We calculate the pressure drop using two methods: measuring the average number of particles turned around per iteration (per unit time) by the 'gravitational force' and counting the average number of collisions with the wall per iteration, as already discussed in Section 3. In the case of a steady-state flow, both of them have to converge to the same value. If this is so, it can be used as an indication that the rough wall does not disturb the momentum transfer from the bulk to the surface and that the bulk flow is truly hydrodynamic. This does not mean that LGA can reproduce the real hydrodynamics even inside the smallest pores, but this does not affect the bulk flow. In Table I we summarize the results for some of the studied cases.

The numbers in columns three and four are the average of 60000 iterations. The difference between the force calculated as the average applied force and that

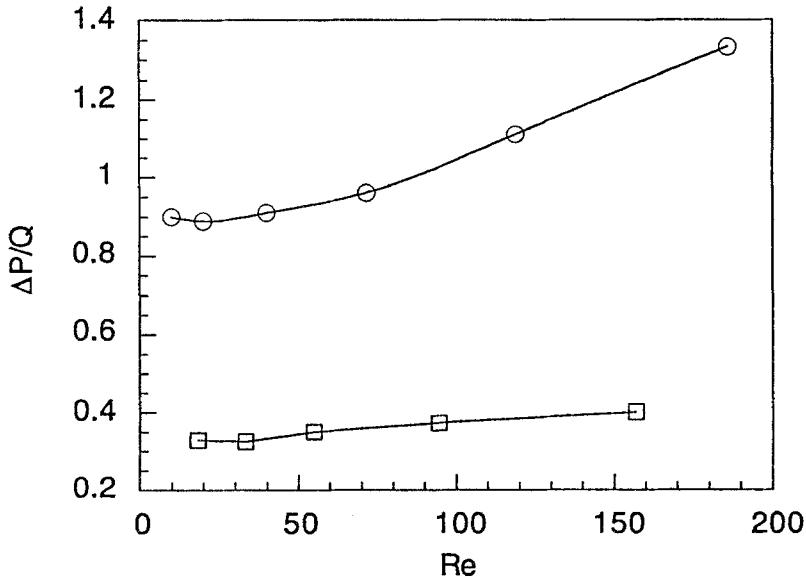


Fig. 11. $\Delta P/Q$ vs. Re for the rough channel of Figure 12 (circles) and for a smooth channel (squares) of 600 lattice units length. Note that for large Re numbers the rough channel clearly deviates from the constant $\Delta P/Q$ ratio predicted by Equation (1), whereas in the same range of Reynolds numbers, the behavior in the smooth channel shows just a small deviation. (In the rough channel the largest observed $\Delta P/Q$ ratios are 50% larger than the values observed for the low Re numbers whereas in the smooth channel this deviation is approximately 15%.)

calculated as the average friction losses is less than 1% in almost all the cases. Objects with very low H value ($H = 0.3$, Figure 7a) present very narrow pores where hydrodynamic correlations do not develop. On the contrary, objects with large H value ($H = 0.7$, Figure 7c) present wide openings where the streamlines penetrate and the method can be applied even to study the flow pattern in these zones. Although the systems present very different microstructure due to the differences in their roughness exponent H , their permeability can be represented by the same function of the geometry which is also independent of the exponent H – see Equation (11).

5. Non Linearities

The approach used in Section 4 to study the permeability of fracture joints supposes that pressure drop and velocity are linearly related. However, due to the presence of surface irregularities one observes non-linear effects at lower Reynolds numbers than in smooth channels. LGA leads to the incompressible Navier–Stokes equations only in the limit of low Mach numbers, $M = u/u_s$, where u_s is the sound velocity in the lattice. In the case of FHP II model, $u_s = \sqrt{3/7}$ [29], so in our simulations we keep velocities low; the maximum velocity (in the constriction zones) is $u \sim 0.30$ for the largest Reynolds numbers we have studied.

TABLE I. Comparison of force calculated as momentum gain per iteration and as momentum loss per iteration

$H = 0.3$			
$\delta_{av}/2y_{max}$	Re Number	Applied force (lattice units)	Friction losses (lattice units)
1.33	15	1.306	1.302
1.33	50	2.100	2.104
1.66	16	0.232	0.230
1.66	50.5	0.850	0.845
2.32	23	0.116	0.115
2.32	81	0.426	0.426
$H = 0.5$			
$\delta_{av}/2y_{max}$	Re Number	Applied force (lattice units)	Friction losses (lattice units)
1.34	11	0.473	0.470
1.34	44	2.173	2.168
1.75	27	0.461	0.459
1.75	107	2.277	2.274
2.50	45	0.225	0.223
2.50	135	0.786	0.764
$H = 0.7$			
$\delta_{av}/2y_{max}$	Re Number	Applied force (lattice units)	Friction losses (lattice units)
1.36	12	0.473	0.475
1.36	48	2.176	2.183
1.71	26	0.462	0.465
1.71	62	1.265	1.266
2.42	43	0.230	0.226
2.42	125	0.803	0.806

In the flow through a rough channel, one can find deviations from linearity as it is shown in Figure 11 where $\Delta P/Q$ vs. Re number is plotted for the rough channel of Figure 12 and for a smooth channel. We have increased the average width of the rough channel in comparison to those used in the previous section ($\delta_{av} = 640\sqrt{3}/2$ lattice units and $y_{max} = 200\sqrt{3}/2$ lattice units). This enables us to work with larger Reynolds numbers, yet being far below the sound velocity. The flow rates shown in Figure 11 correspond to Reynolds numbers ranging from 20 to 180. For comparison we show in the same figure the behavior of a smooth channel over approximately the same range of Reynolds numbers. The rough channel largely deviates from the linear regime predicted by Darcy law (a constant $\Delta P/Q$ ratio), whereas the

smooth channel behavior approximately remains linear, as can be seen in Figure 11.

Although an asymptotic regime described by a power law of the type $Q \sim (\Delta P)^\alpha$ with $\alpha \neq 1$ could not be reached, it is clear from Figure 11 that surface roughness can be an important source of non-linear effects in the flow through fracture joints. The cause of the deviations is probably the high vorticity zones originated behind obstacles. These zones usually grow when the Reynolds number increases, i.e. the streamlines follow less the surface behind the obstacles (see Figure 12). Due to this effect, the hydraulic diameter is itself a function of the Re number and Eq. (10) is not longer valid. Larger Reynolds numbers can be investigated increasing the channel width but keeping the same relative roughness. This will enable us to work at larger Reynolds numbers while the maximum velocity remains constant. This study can answer the question about a power law behavior with an exponent that can be a function of the roughness. However, this is beyond our computer capabilities at this moment.

6. Conclusion

We have shown that LGA simulations can constitute a powerful tool in the study of hydrodynamics in fracture joints. We have studied the permeability problem in the linear and nonlinear regime. The studied system has no analytical solution. As a result, the appropriateness of the method cannot be analyzed comparing numerical to analytical results as it has been done for other cases [20, 23]. We have shown that LGA reproduce expected results for the hydrodynamic permeability. The permeability is fully determined in terms of the relative surface roughness and it is independent of the roughness exponent H . A transition to a regime in which the system is not longer described by the linear Darcy equation has also been observed. This transition occurs in a regime in which the behavior in a smooth channel remains linear.

A natural extension of this work, would be to seek solutions of boundary layer problems in the presence of surface roughness, and to study tracer dispersion in channels with rough walls. Both of these problems are of great importance in many industrial applications. They are furthermore, both eminently suited for the LGA method. We are at present working on these problems. Further extensions (as suggested by an anonymous referee) include studies of flow permeability in 3D fractures. In order to compare the results of the present work with 3D simulations one has to relate the aperture distribution along flow paths (which can probably be approximated as 2D) to the global fracture aperture distribution, as flow preferentially occurs in wide aperture areas, avoiding asperities and contact zones.

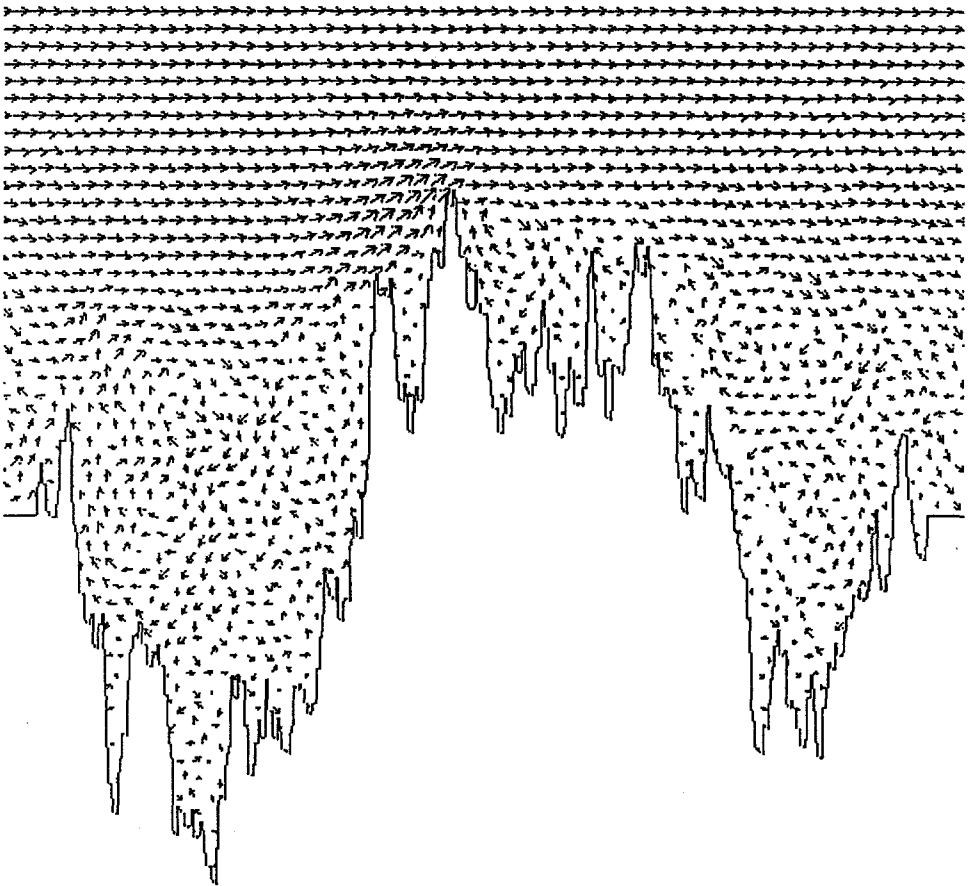


Fig. 12. Fluid-flow in a rough channel. The roughness exponent of the surface is $H = 0.5$, $\delta_{av} = 640$ lattice units, $y_{max} = 200$ lattice units, $Q = 30$ and the Reynolds number $Re = 115$. The large zones behind the obstacles are probably the origin of the nonlinear behaviour. The strength of the flow field is shown in a logarithmic scale (see footnote in Section 4b).

Acknowledgments

We thank E. G. Flekkøy for valuable comments and discussions during the early parts of this work. We also thank the C.I.R.C.E., the C.C.V.R. and I.D.R.I.S. for computer time on their Fujitsu VP200, Cray 2 and Cray C98. We thank the G.D.R. 'Physique de Milieux Hétérogènes Complexes' of C.N.R.S. for financial support.

References

1. Mandelbrot, B. B., Passoja, D. E. and Paullay, A. J., *Nature* **308** (1984) 721.
2. Brown, S. R. and Scholz, C. H., *J. Geophys. Research* **90** (1985) 12575.

3. Power, W. L., Tullis, T. E., Brown, S. R., Boitnott, G. N. and Scholz, C. H., *Geophys. Res. Lett.* **14** (1987) 29.
4. Mu, Z. Q. and Lung, C. W., *J. Phys. D* **21** (1988) 848.
5. Mecholsky, J. J., Passoja, D. E. and Feinberg-Ringel, K., *J. Am. Ceram. Soc.* **72** (1989) 60.
6. Bouchaud, E., Lapasset, G. and Planès, J., *Europhys. Lett.* **13** (1990) 73.
7. Bursill, L. A., Fan XuDong and Peng Julin, *Philos. Mag. A* **64** (1991) 443.
8. Måløy, K. J., Hansen, A., Hinrichsen, E. L. and Roux, S., *Phys. Rev. Lett.* **68** (1992) 213.
9. Tanaka, M., *J. Mater. Sci.* **27** (1992) 4717.
10. Issa, M. A., Hammad, A. M. and Chudnovsky, A., in *Engineering Mechanics* (ed.) by L. D. Lutes and J. M. Niedzwecki (American Soc. of Civil Engineers, New York, 1992).
11. Schmittbuhl, J., Gentier S. and Roux, S., *Geophys. Res. Lett.* **20** (1993) 639.
12. Milman, Yu. V., Blumenfeld, R., Stelmanshenko, N. A. and Ball, R., *Phys. Rev. Lett.* **71** (1993) 204.
13. Bouchaud, E., Lapasset, G., Planès, J. and Naveos, S., *Phys. Rev. B* **48** (1993) 2917.
14. Horvath, V., Kertész, J. and Weber, F., *Fractals* **1** (1993) 67.
15. Engøy, T., Måløy, K. J., Hansen, A. and Roux, S., *Phys. Rev. Lett.* **73** (1994) 834.
16. See e.g. Tzschichholz, F. and Pfuff, M., in J. G. M. van Mier, J. G. Rots and A. Bakker (ed.) *Fracture Processes in Concrete, Rock and Ceramics*, Vol. 1, Cambridge University Press, Cambridge, 1991; Lea Cox, B. and Wang, J. S. Y., *Fractals* **1** (1993) 87; or Bouchaud E. in the Proceedings of the conference 'Dislocations 93' for reviews.
17. Feder, J., *Fractals* Plenum, New York, 1988.
18. Frisch, U., Hasslacher, B. and Pomeau, Y., *Phys. Rev. Lett.* **56** (1986) 1505.
19. Rothman, D. H., *Geophysics* **53** (1988) 509.
20. Flekkøy, E. G., Feder, J. and Jøssang, T., *J. Stat. Phys.* **68** (1992) 515.
21. Rothman, D. H. and Keller, J. M., *J. Stat. Phys.* **52** (1988) 1119.
22. Gunstensen, A. K., Rothman, D. H., Zaleski, S. and Zanetti, G., *Phys. Rev. A* **43** (1991) 4320.
23. Lim, H. A., *Phys. Rev. A* **40** (1989) 968
24. Tsang, Y. W., Witherspoon, P. A., *J. Geophys. Res.* **86** (1981) 9287.
25. Schrauf, T. W. and Evans, D. D., *Water Resour. Res.* **22** (1986) 1038.
26. Brown, S. R., *J. Geophys. Res.* **92** (1987) 1337.
27. Roux, S., Schmittbul, J., Vilotte, J. P. and Hansen, A., *Europhys. Lett.* **23** (1993) 27.
28. Frisch, U., d'Humières, D., Hasslacher, B., Lallemand, P., Pomeau, Y. and Rivet, J. P., *Complex Systems* **1** (1987) 649.
29. d'Humières, D. and Lallemand, P., *Physica* **140A** (1986) 326.
30. Brosa, U. and Stauffer, D., *J. Stat. Phys.* **57** (1989) 399.
31. Clavin, P., d'Humières, D., Lallemand, P. and Pomeau, Y., *C. R. Acad. Sc. Paris* **303**(II) (1986) 1169.
32. Voss, R. F., *Random fractal forgeries*, in R. A. Earnshaw (ed.) *Fundamental Algorithm in Computer Graphics*, Springer Verlag, Berlin, 1985, p. 805.
33. Kohring, G. A., *J. Stat. Phys.* **63** (1991) 411.
34. Kohring, G. A., *J. Phys. II* (Paris) **1** (1991) 593.